On the Crossover of Boundary Currents in an Idealized Model of the Red Sea

PING ZHAI

MIT–WHOI Joint Program in Physical Oceanography, Woods Hole Oceanographic Institution, Woods Hole, Massachusetts, and Department of Marine, Earth and Atmospheric Sciences, North Carolina State University, Raleigh, North Carolina

LARRY J. PRATT AND AMY BOWER

Department of Physical Oceanography, Woods Hole Oceanographic Institution, Woods Hole, Massachusetts

(Manuscript received 15 September 2014, in final form 27 January 2015)

ABSTRACT

The west-to-east crossover of boundary currents has been seen in mean circulation schemes from several past models of the Red Sea. This study investigates the mechanisms that produce and control the crossover in an idealized, eddy-resolving numerical model of the Red Sea. The authors also review the observational evidence and derive an analytical estimate for the crossover latitude. The surface buoyancy loss increases northward in the idealized model, and the resultant mean circulation consists of an anticyclonic gyre in the south and a cyclonic gyre in the north. In the midbasin, the northward surface flow crosses from the western boundary to the eastern boundary. Numerical experiments with different parameters indicate that the crossover latitude of the boundary currents changes with f_0, β, and the meridional gradient of surface buoyancy forcing. In the analytical estimate, which is based on quasigeostrophic, β-plane dynamics, the crossover is predicted to lie at the latitude where the net potential vorticity advection (including an eddy component) is zero. Various terms in the potential vorticity budget can be estimated using a buoyancy budget, a thermal wind balance, and a parameterization of baroclinic instability.

1. Introduction

The Red Sea is an example of an ''inverse estuary'' in which surface buoyancy loss far exceeds the gain because of freshwater input. It differs from the Mediterranean Sea and from other prominent marginal seas in its narrow and meridionally elongated geometry. In fact, its latitude range is such that the Coriolis parameter f doubles from the south to the north tip, resulting in a novel situation in which zonal motion is encouraged by a strong beta effect but suppressed by narrow geometry.

Observations of the Red Sea circulation are temporally and spatially sparse, and many properties of the climatological circulation are uncertain. Robust features include the overturning circulation, which occupies the upper 300 m in the north and upper 150 m in the south and whose annual transport of about 0.36 Sverdrups (Sv; $1\ \text{Sv} = 10^6\ \text{m}^3\ \text{s}^{-1}$) is based on measurements within the strait of Bab el Mandeb (BAM) (Murray and Johns 1997). There is also striking transition in summer to a three-layer exchange flow in the BAM, which is thought to be because of the summer reversal in the wind direction in the southern Red Sea and Gulf of Aden as well as in the Arabian Sea (Smeed 1997, 2000, 2004; Yao et al. 2014a,b). Another feature that appears in multiple observations is a cyclonic gyre, approximately 300 m deep, at the northern end (Vercelli 1927; Morcos 1970; Morcos and Soliman 1974; Maillard 1974; Clifford et al. 1997), believed to be a site of convection and Red Sea overflow water production (Sofianos and Johns 2003). Many inferences about the general circulation come from numerical simulations (e.g., Clifford et al. 1997; Eshel and Naik 1997; Siddall et al. 2002; Sofianos et al. 2002; Sofianos and Johns 2003; Biton et al. 2008, 2010; Chen et al. 2014; Yao et al. 2014a,b), most of which reproduce the northernmost gyre but which can differ in other aspects. There have been very few analytical models, laboratory experiments,

Corresponding author address: Ping Zhai, Department of Marine, Earth and Atmospheric Sciences, North Carolina State University, Jordan Hall, RM 4145, Raleigh, NC 27695-8208.
E-mail: pingzhai425@gmail.com

DOI: 10.1175/JPO-D-14-0192.1

or idealized numerical simulations apart from the celebrated Phillips (1966) model, but his restriction to a two-dimensional overturning cell and his neglect of rotation are limiting.

An interesting feature of the three-dimensional, time-mean winter circulation captured in the models of Sofianos and Johns (2003) and Yao et al. (2014b) is a zonal jet or crossing flow that lies near the Red Sea midlatitude. In these simulations, surface water that enters the Red Sea from the BAM forms a northward western boundary current. This current can be seen in the Sofianos and Johns (2003) 9-yr average, shown here in Fig. 1. When the current reaches 19°N it sharply veers to the east and crosses to the eastern boundary, where it continues northward. (The crossover can also be seen at the bottom of Fig. 6 in Yao et al. 2014b). There is also indirect observational evidence for such a crossover from sea surface temperature fields, as discussed below. The crossover jet appears in the time mean but may not show up clearly in instantaneous realizations of the flow field, which typically contain multiple eddies and small gyres (e.g., Quadfasel and Baudner 1993; Zhai and Bower 2013; Chen et al. 2014). It is perhaps not surprising then that the crossover is identified only in modeling works that show the time average over multiple years.

Observational evidence for the crossover is weaker, partly because it is difficult to make measurements of the time mean. There are very few time series of velocity at fixed locations, so the calculation of a mean circulation from in situ observations is out of the question. Furthermore, the relatively sparse hydrographic measurements in the Red Sea mean it is not possible to construct maps of absolute dynamic topography from altimetry, as is done in other ocean basins (www.aviso.oceanobs.com/en/data/products/auxiliary-products/mdt). We can, however, examine evidence inferred from satellite sea surface temperature (SST). SST can be determined from satellite remote sensing using microwave (MW) and infrared (IR) radiometers. The merged MW–IR SST product takes maximum advantage of the greater coverage of MW and higher resolution of IR. This product is distributed on a 0.09° grid and covers data from January 2006 to present. Figure 2 shows the climatological SST for December. There is a warm tongue along the eastern boundary in the northern Red Sea, a feature that could be indicative of a northward boundary current along the eastern boundary. This warm tongue continues along the western boundary in the northern Red Sea, which implies that there is a southward boundary current along the western boundary in the north. There is also cool tongue along the western boundary in the south, suggesting a

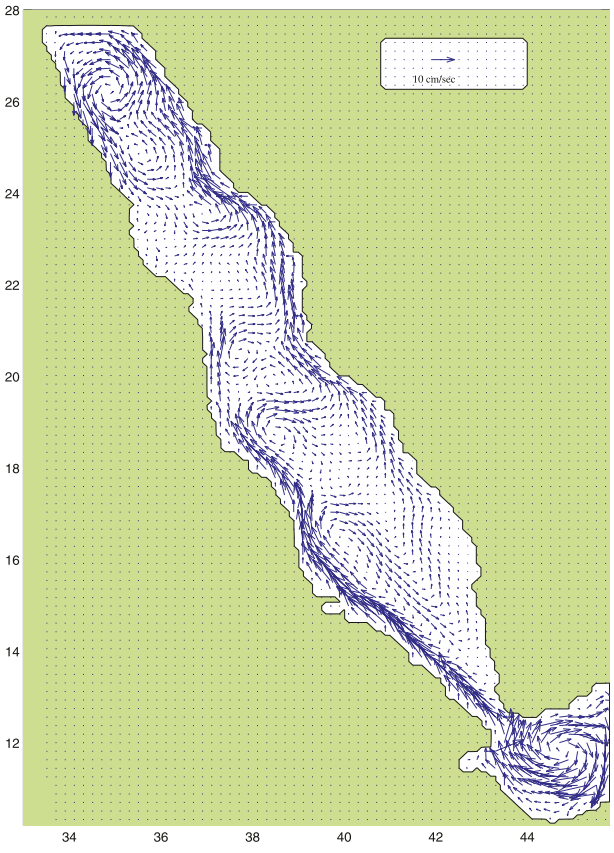

FIG. 1. The 9-yr average surface current driven by surface buoyancy forcing using the Miami Isopycnal Coordinate Ocean Model (MICOM) (Sofianos and Johns 2003, their Fig. 15).

northward flow from the strait of Bab el Mandeb along the western coast. This northward western boundary current turns eastward and crosses the basin at 20°N, about the same latitude of the crossover jet in Fig. 1. Although these SST features do not necessarily indicate a flow direction, they are suggestive of cyclonic boundary currents in the northern Red Sea and a northwestward western boundary current in the southern Red Sea.

In summary, the crossover jet appears in the time-mean surface circulation of two independent models and its presence is consistent, though not directly confirmed, with observations of SST. It is of interest, therefore, to probe further and ask whether the crossover is a generic feature of circulation in a meridionally elongated, buoyancy-forced basin with strong beta effect. We note that the crossover is not a feature of idealized *f*-plane models of buoyancy-driven marginal sea circulation (e.g., Spall 2004; Pratt and Spall 2008), suggesting that the beta effect is important. However, we will argue that it does occur, and is robust, when the beta effect is present and when the basin is given the elongated geometry of the Red Sea. We

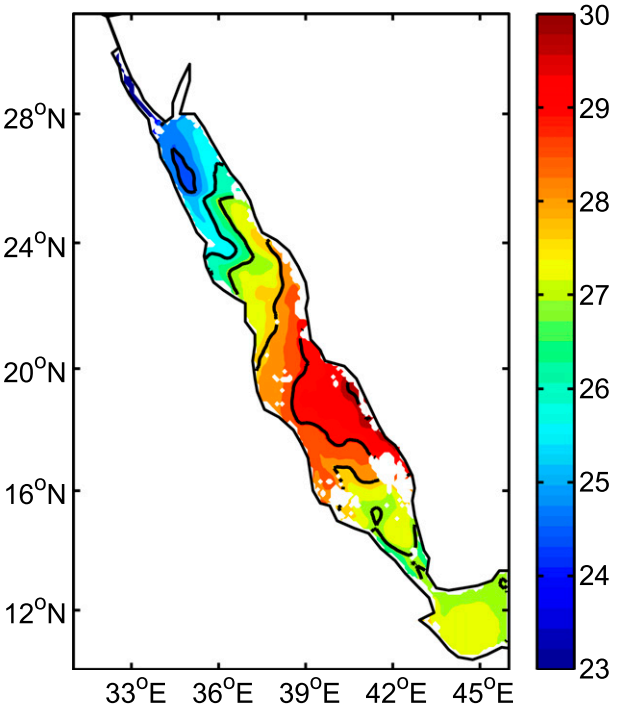

FIG. 2. Climatological MW–IR SST (°C) for December.

will also show that the crossover depends on the presence of a northward increase in the surface buoyancy flux, also a feature of the Red Sea air–sea interaction. We will explore the dynamics of the crossover and present an analytical estimate of its latitude as a function of f_0, β, and the northward gradient of the surface buoyancy flux. This work is organized as follows: Section 2 describes the numerical simulation of the buoyancy-driven circulation in an idealized Red Sea using an eddy-resolving general circulation model. Section 3 introduces an ad hoc analytical estimate, centered on the buoyancy equation and on potential vorticity dynamics, of parameter dependencies of the crossover latitude. Section 4 offers some conclusions.

2. Numerical model simulation of the buoyancy-driven circulation in an idealized Red Sea

a. Model description

The Massachusetts Institute of Technology general circulation model (MITgcm) (Marshall et al. 1997) is used to simulate the buoyancy-driven circulation in an idealized Red Sea. The model used in this study is nonhydrostatic and solves the momentum and density equations on a Cartesian, staggered Arakawa C grid. The parameters that are used in the control experiment (EXPT0) are described in this section, whereas parameter settings for other experiments are listed in Table 1. The model domain includes the idealized Red Sea, the strait of Bab el Mandeb, and the Gulf of Aden (Fig. 3). The idealized Red Sea is a rectangular basin with a width of 300 km and a length of 1600 km. The Gulf of Aden is 600 km wide and 250 km long. In the Red Sea and the Gulf of Aden, the bottom depth increases from 0 m at the coast to 1000 m over an offshore distance of 80 km. The strait of Bab el Mandeb is 100 km wide and 150 km long, with a sill depth of 200 m. The horizontal grid spacing is 5 km, and there are 29 vertical levels, with thickness varying from 10 m at the surface to 100 m at the bottom. The Coriolis parameter in EXPT0 is approximated by $f = f_0 + \beta y$ with $f_0 = 3.5 \times 10^{-5}\,\mathrm{s}^{-1}$ and $\beta = 2.1 \times 10^{-11}\,\mathrm{m}^{-1}\,\mathrm{s}^{-1}$, which are typical of the Red Sea. The term f_0 is the Coriolis parameter at the southern boundary of the model domain.

The model is forced by surface fluxes of heat Q and freshwater E in the Red Sea. In EXPT0, Q changes linearly from 0 at the southern end of the Red Sea ($y = 400$ km) to $-20\,\mathrm{W\,m}^{-2}$ at the northern end

TABLE 1. Model run parameters and symbols used in Fig. 13. $B_0 = ay + b$ represents the surface buoyancy flux, and Y_C is the crossover latitude. Units are B_0 ($\mathrm{kg\,m}^{-2}\,\mathrm{s}^{-1}$); f_0 (s^{-1}); β ($\mathrm{m}^{-1}\,\mathrm{s}^{-1}$); a ($\mathrm{kg\,m}^{-3}\,\mathrm{s}^{-1}$); b ($\mathrm{kg\,m}^{-2}\,\mathrm{s}^{-1}$); and crossover Y_C (km).

EXPT	f_0 ($\times 10^{-5}$)	β ($\times 10^{-11}$)	a ($\times 10^{-12}$)	b ($\times 10^{-6}$)	Y_C	Symbol
EXPT0	3.5	2.1	3.5	−1.4	1028	Δ
EXPT1	1.5	2.1	3.5	−1.4	1351	●
EXPT2	2.5	2.1	3.5	−1.4	1139	●
EXPT3	7.0	2.1	3.5	−1.4	798	●
EXPT4	10.5	2.1	3.5	−1.4	674	●
EXPT5	3.5	0.5	3.5	−1.4	852	Δ
EXPT6	3.5	1.5	3.5	−1.4	995	Δ
EXPT7	3.5	4	3.5	−1.4	1152	Δ
EXPT8	3.5	6	3.5	−1.4	1218	Δ
EXPT9	3.5	2.1	0	2.8	658	O
EXPT10	3.5	2.1	1.7	0.7	927	O
EXPT11	3.5	2.1	2.6	−0.34	989	O
EXPT12	3.5	2.1	4.3	−2.4	1074	O

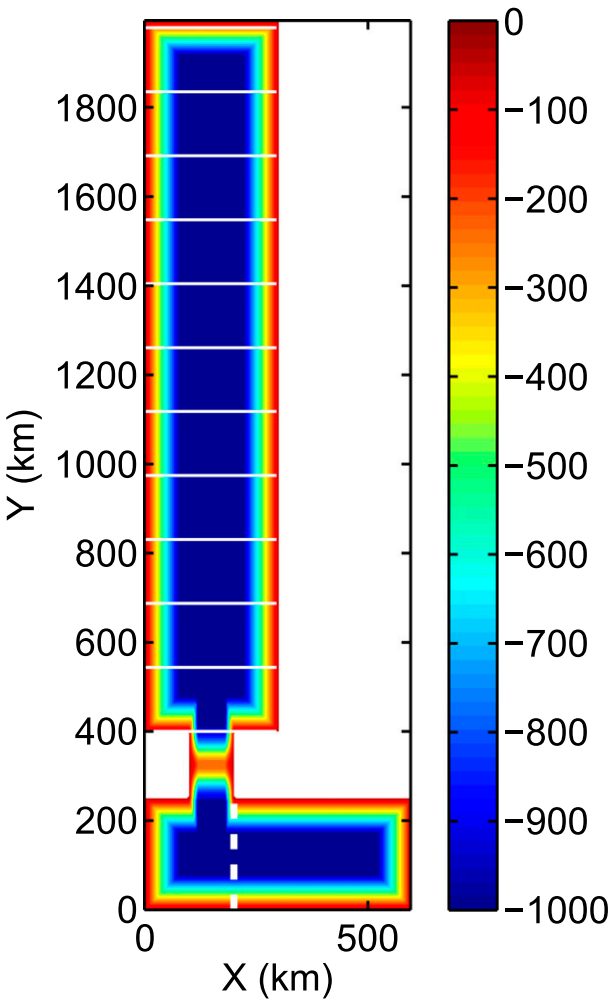

FIG. 3. Model domain with bottom topography (colors, m) and EXPT0 surface buoyancy loss (white contours with contour interval of $0.5 \times 10^{-6}\,\mathrm{kg\,m^{-2}\,s^{-1}}$ and with zero contour at $Y = 400\,\mathrm{km}$). Temperature and salinity in the region east of the dashed white line are restored to the initial profiles.

($y = 2000\,\mathrm{km}$), and E increases linearly from 0 at the southern end of the Red Sea to $4.3\,\mathrm{m\,yr^{-1}}$ at the northern end. We use a linear equation of state, such that $\rho = \rho_r(1 - \alpha_T T + \beta_S S)$, where $\rho_r = 999.8\,\mathrm{kg\,m^{-3}}$ is a reference density and $\alpha_T = 2 \times 10^{-4}\,^{\circ}\mathrm{C}^{-1}$ and $\beta_S = 8 \times 10^{-4}$ are thermal expansion and haline contraction coefficients. The surface buoyancy flux (Fig. 3) calculated from Q and E is $B_0 = -\alpha_T Q/c_w + \rho_0 \beta_S S_0 E$, where $c_w = 3900\,\mathrm{J\,kg^{-1}\,^{\circ}C^{-1}}$ is the heat capacity of water. In this model, surface freshwater flux changes the salinity of seawater but cannot affect the total volume. The buoyancy flux B_0 has units of kilograms per square meter per second and increases linearly with latitude according to $B_0 = ay + b$ (Table 1).

In the numerical experiments shown in Table 1, the mean buoyancy flux over the whole Red Sea remains fixed. We will be particularly interested in how the mean circulation is affected by variations in the distribution of the surface buoyancy flux and in f_0 and β. The initial conditions for temperature and salinity are based on average profiles of temperature and salinity measured from the March 2010 and September–October 2011 Red Sea cruises (Bower 2010; Bower and Abualnaja 2011; Bower and Farrar 2015). The temperature and salinity in the eastern part of the Gulf of Aden (Fig. 3) are relaxed to these initial profiles with a relaxation time scale of 60 days. We have tried different relaxation profiles in the eastern Gulf of Aden and different choices of relaxation profiles do not influence the circulation pattern. The relaxation of temperature and salinity in the Gulf of Aden acts as a source of buoyancy to balance the surface buoyancy losses in the Red Sea. Second-order viscosity and diffusivity are used to parameterize subgrid-scale processes. In the area outside the strait and west from the buffer zone, the surface buoyancy flux is zero. The vertical viscosity and diffusivity for temperature and salinity are $10^{-5}\,\mathrm{m^2\,s^{-1}}$. The vertical diffusivity is increased to $1000\,\mathrm{m^2\,s^{-1}}$ when the water column is hydrostatically unstable in order to simulate convection. There is no explicit horizontal diffusivity of temperature and salinity in the model. The Smagorinsky viscosity ν_S is used to determine the horizontal viscosity, such that $A_h = (\nu_S/\pi)^2 L^2 \sqrt{(u_x - v_y)^2 + (u_y + v_x)^2}$, where L is the spacing scale, u and v are horizontal velocities, and subscripts represent partial derivatives. Recommended values for ν_S are in the range of 2.2 to 4 for large-scale oceanic simulations (Griffies and Hallberg 2000); we have chosen $\nu_S = 2.5$. No slip boundary conditions are applied at bottom and lateral boundaries.

The model is run for 25 yr with steady surface heat loss and evaporation and reaches a quasi-steady state. Unless it is explicitly stated otherwise, the mean fields discussed in this study will be the average over the final 5 yr of the 25-yr simulation.

b. *Numerical model results*

The benchmark experiment EXPT0 reveals a set of gyres and boundary currents that establish pathways for the northward movement of lighter water from the strait through the Red Sea basin. As indicated in Fig. 4, which shows a 5-yr mean surface velocity and density, the surface inflow from the Gulf of Aden brings lighter water into the Red Sea through the strait of Bab el Mandeb. When the inflow enters the Red Sea, it turns left and continues moving northward along the western boundary until it reaches about 1000 km, where it turns east and crosses the basin. Because of the surface buoyancy losses, the density of each boundary current increases as the inflow moves northward. To the north of the crossover

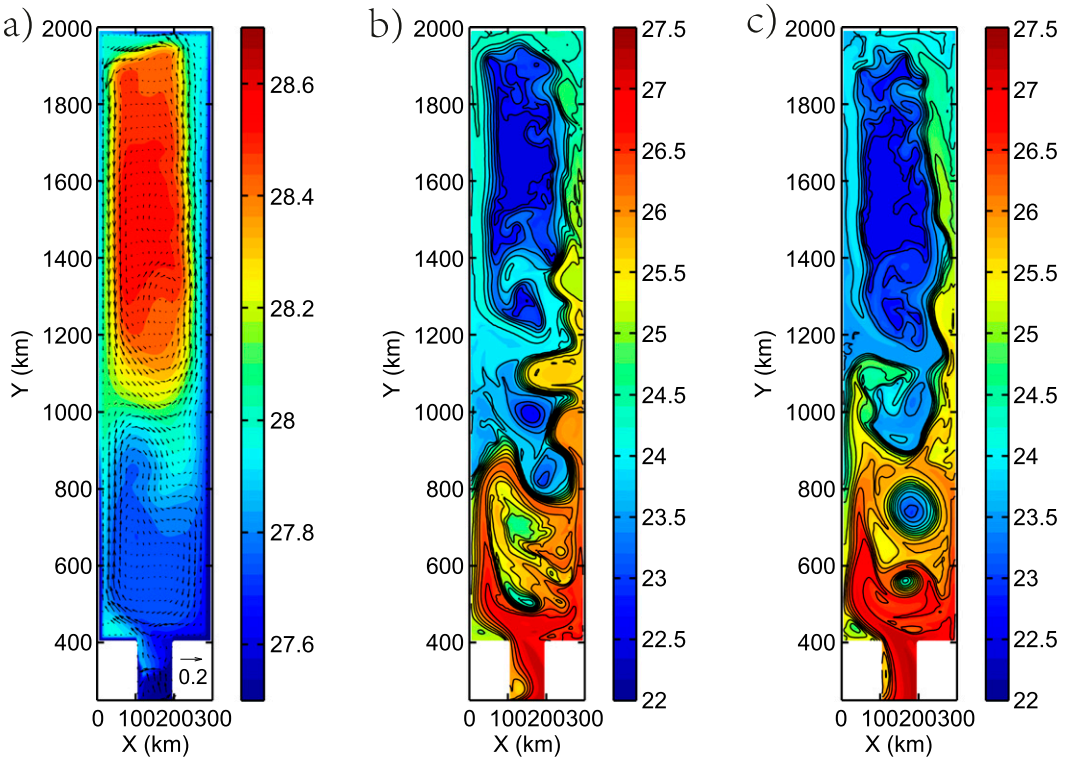

FIG. 4. (a) Mean density (kg m^{-3}) and horizontal velocity (m s^{-1}) for EXPT0 averaged over the upper 200 m. (b),(c) Two snapshots of the surface temperature from EXPT0 (contour interval is 0.3°C).

latitude, the surface boundary circulation is cyclonic; in the southern Red Sea, it is predominantly anticyclonic. Two snapshots of the surface temperature (Fig. 4) from EXPT0 suggest the same general configuration of boundary currents and crossover as in the 5-yr mean fields. Eddies are also present in the snapshots, and the crossover in one snapshot occurs slightly to the south of its mean position near 1000 km, while the crossover in another snapshot occurs to the north of its mean position. The eddies may be instrumental in transporting warm and freshwater from the boundary currents to the interior where heat and freshwater are lost because of surface cooling and evaporation, as described by Spall's 2004 *f*-plane experiment.

The zonal sections of meridional velocity at $y = 500$ and 1770 km are plotted in Fig. 5. The vertical structure of the meridional velocity at $y = 1770$ km indicates that the cyclonic boundary circulation in the northern Red Sea is intensified in the upper 200 m with maximum speed in excess of 30 cm s^{-1}. Recall that 200 m is also the sill depth for the southern strait. Below 200 m, there is a much weaker anticyclonic circulation with speed less than 5 cm s^{-1}. The zonal section of meridional velocity at $y = 500$ km indicates that the circulation in the southern Red Sea is also intensified in the upper 200 m. The western boundary current can extend to 800 m. However its speed below 200 m is very weak. The weaker, northward-flowing eastern boundary current only penetrates down to 100 m and overlies a countercurrent that extends from 100 to 300 m and is situated slightly offshore. The maximum velocity of the surface northward flow is about 5 cm s^{-1} and that of the subsurface southward countercurrent is about 10 cm s^{-1}. The countercurrent returns water in the Red Sea back to the strait. Therefore, the vertical, integrated boundary current on the eastern boundary is southward and the depth-integrated circulation in the southern Red Sea is predominantly anticyclonic. Overall, the surface circulation associated with waters entering the model domain through the strait is stronger than the intermediate circulation that carries the return flow. The primary reason for this mismatch is the presence of a strong recirculation component in the surface flow, especially in the northern basin.

The determination of the crossover latitude of the northward western boundary current in the numerical model is illustrated in Fig. 6. The crossover latitude is defined as the zero-crossing point of the mean meridional velocity on the western boundary, taken as the average meridional velocity within 80 km of the western coast and

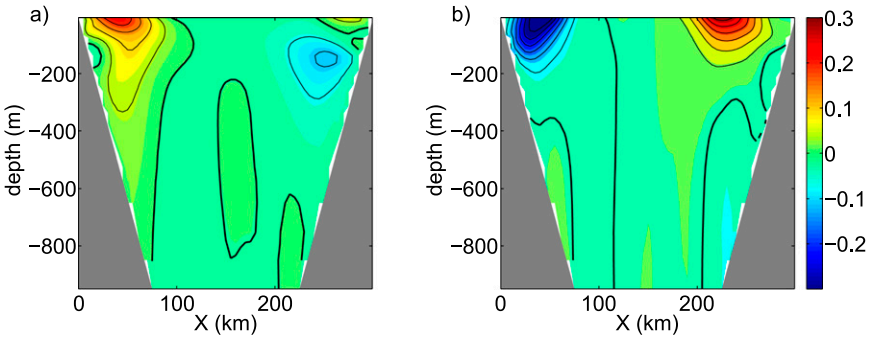

FIG. 5. Zonal sections of mean meridional velocity (contour interval is 5 cm s^{-1}) from EXPT0 at (a) $y = 500$ km and (b) $y = 1770$ km. Zero velocity contour is plotted in thick black lines.

in the upper 200 m. (In our model, 80 km is the offshore topographic width scale and also the approximate width of the boundary current.) In EXPT0, the crossover latitude of the western boundary is 1028 km. Subsequent numerical experiments with different parameters will indicate that the crossover latitude varies with f_0, β, and the meridional gradient of surface buoyancy fluxes. As shown in Table 1 and Fig. 7, the crossover latitude moves to 1351 km when $f_0 = 1.5 \times 10^{-5}\,s^{-1}$ (EXPT1) or to 1218 km when β is increased to $6 \times 10^{-11}\,m^{-1}\,s^{-1}$ (EXPT8). In EXPT10, the meridional gradient of surface buoyancy flux is reduced, and the crossover latitude shifts to 927 km.

Sofianos and Johns (2003) suggested that crossover occurs at the latitude above which Rossby waves with the frequency of the forcing ($2\pi\,yr^{-1}$ in their study) are no longer possible and only Kelvin waves exist. Their argument is based on a study of eastern boundary currents by McCreary et al. (1986, hereinafter MSK86), in which a subtropical ocean is subject to time-periodic, wind, and buoyancy forcing at frequency σ. The critical latitude for a long Rossby wave with this frequency, and with vertical mode number n, is shown to be $\theta_{cr} = \tan^{-1}[c_n/(2R\sigma)]$, where R is Earth's radius. Poleward of θ_{cr}, this wave becomes Kelvin-like, decaying away from the eastern boundary over the Rossby radius of deformation. The argument then is that western boundary layer dynamics should prevail at the annual frequency south of θ_{cr}, while an eastern boundary layer should exist to the north. Sofianos and Johns (2003) find reasonable agreement between their observed crossover latitude and the value of θ_{cr} obtained by choosing σ as the seasonal frequency ($2\pi\,yr^{-1}$) and by choosing the second baroclinic mode ($n = 2$) and computing the associated vertical eigenvalue c_n. One difficulty with this approach is that the crossover exists in our model (and in that of Yao et al. 2014b) in the presence of steady forcing. For this case, $\sigma = 0$, and the above prediction would put the crossover at 90°N. In addition, the crossover latitude in the mean field does not change significantly if an annual cycle is substituted for the steady forcing, as illustrated in Fig. 8 for the EXPT0 simulation with and without an annual cycle. It was mentioned in the introduction that the crossover is identified only in a time average over multiple years. Because of the presence of eddies in the instantaneous field, it is difficult to estimate crossover latitude for time periods shorter than a few months. There are some other interesting comparisons with the MSK86, and these will be discussed in the final section.

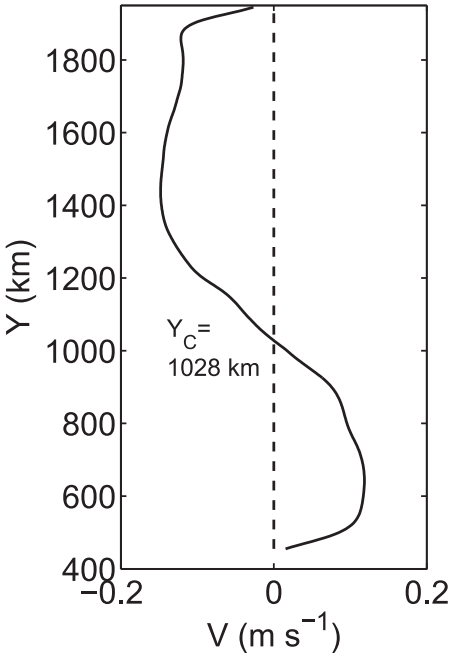

FIG. 6. Mean western boundary current speed, which is calculated as the average meridional velocity in the western boundary (within 80 km of the western boundary) in the upper 200 m. The crossover latitude Y_C is defined as the zero-crossing point.

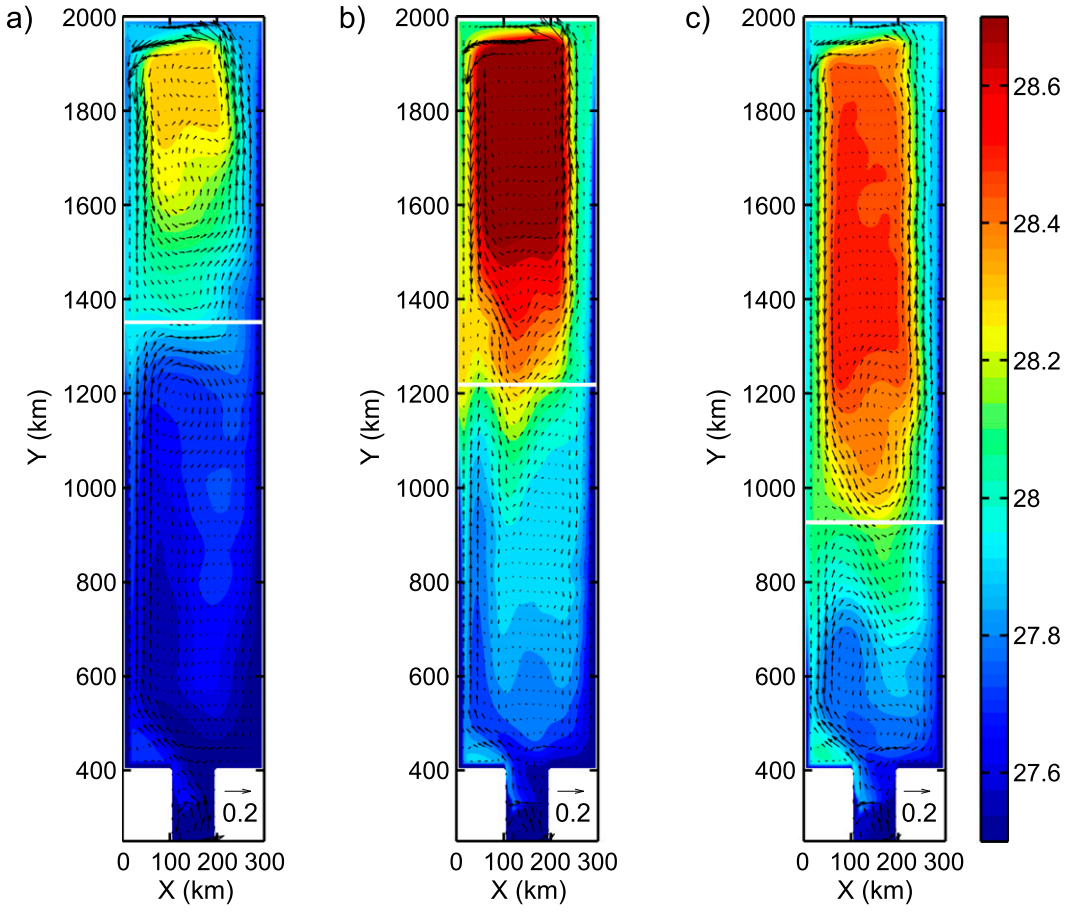

FIG. 7. Mean density (kg m^{-3}) and horizontal velocity (m s^{-1}) averaged over the upper 200 m in (a) EXPT1, (b) EXPT8, and (c) EXPT10. White lines represent crossover latitude estimated using the method shown in Fig. 6.

Buoyancy-driven models of circulation in *f*-plane marginal seas (e.g., Spall 2004) often produce a cyclonic rim current at the surface, with no crossover. We therefore look to the β effect and to other influences, such as the meridional variation of surface buoyancy forcing, to establish a crossover. Both are of potential significance over the large meridional extent of the Red Sea.

3. An analytical prediction of the crossover latitude

The numerical model results in the previous section indicate that the crossover latitude of the northward western boundary current is related to f_0, β, and to the meridional gradient a of the surface buoyancy forcing. In this section, an analytical estimate based on potential vorticity (PV) dynamics is developed. The analytical model is idealized, with some assumptions being ad hoc, and the aim is to further clarify the physics that controls the crossover.

The model describes the horizontal circulation averaged over the depth $H = 200$ m and with a quiescent body of fluid below. In reality, the top 200 m contains elements of the surface inflow and intermediate outflow, but the former dominates the horizontal circulation in most places because of a great prevalence of recirculating components in the surface circulation.

a. *The physics of the crossover*

Consider the quasigeostrophic PV equation for the time-mean flow:

$$\nabla \cdot (\overline{\mathbf{u}}\,\overline{q}) + \frac{\partial}{\partial x}\overline{u'q'} + \frac{\partial}{\partial y}\overline{v'q'} = \frac{\partial Q}{\partial z} + \mathrm{curl}(\mathbf{F}_r) \qquad (1)$$

(e.g., Pedlosky 1996). The PV q of the time-mean flow is given by $q = \beta y + \partial/\partial z[f_0\rho_a/(\partial\rho_b/\partial z)] + \zeta$, where $\zeta = \partial v/\partial x - \partial u/\partial y$. The density field has been partitioned as

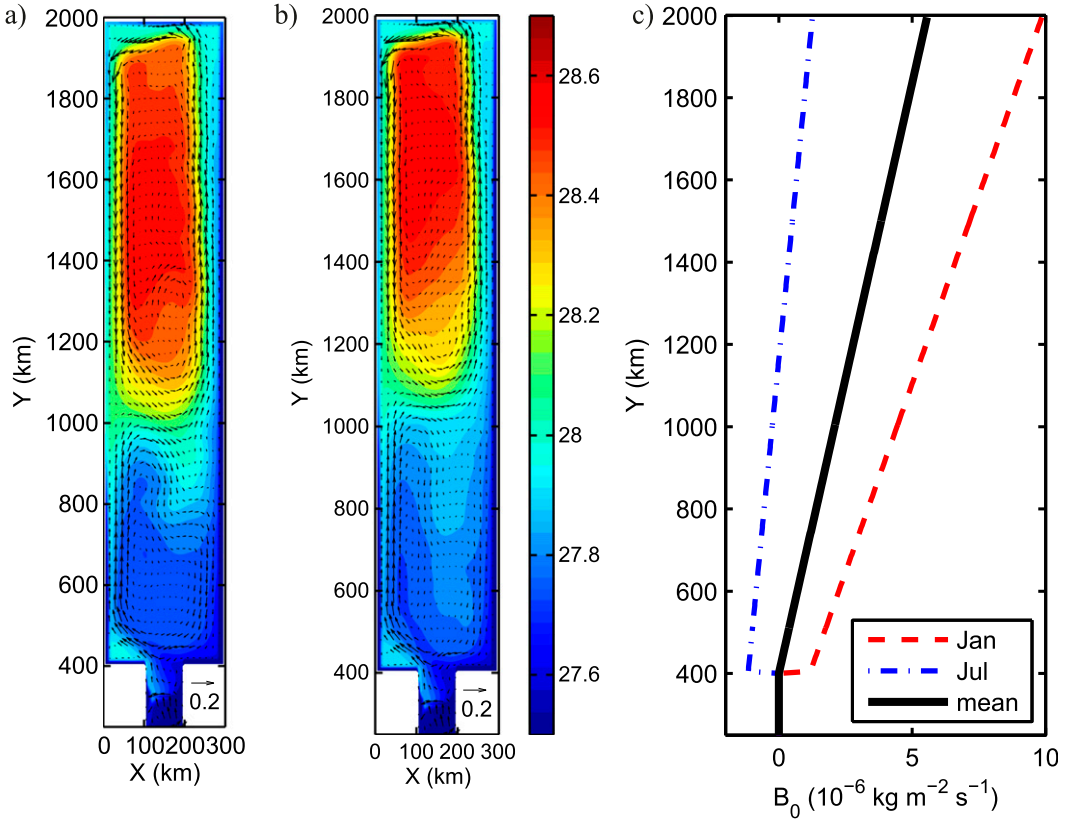

FIG. 8. Mean surface density (kg m^{-3}) and horizontal velocity (m s^{-1}) in (a) EXPT0 with steady forcing and (b) an experiment using surface buoyancy forcing with annual cycle. The surface buoyancy forcing used in (b) has a form of $ay + b + c\cos(t)$. (c) The values in January (maximum) and July (minimum) are plotted. The annual-mean buoyancy forcing indicated by the thick black line is the same as EXPT0.

$\rho(x, y, z) = \rho_b(z) + \rho_a(x, y, z)$, and Q and $\mathbf{F}_r$ represent unspecified heating and friction functions. The overbar represents a time average, and primes are deviations from the time average.

Now integrate (1) over a volume extending throughout the active layers and enclosed by a rectangular circuit C that contains a segment of the western boundary current and extends slightly offshore of its outer edge (Fig. 9):

$$\int_0^L \int_{y_1}^{y_2} \int_{-H}^{0} \left(\frac{\partial \overline{v}\,\overline{q}}{\partial y} + \frac{\partial \overline{v'q'}}{\partial y} + \frac{\partial \overline{u'q'}}{\partial x} \right) dz\, dy\, dx = \iint_{A_C} Q_{z=0}\, dA + \oint_C \int_{-H}^{0} \mathbf{F}_r \cdot dz\, dl\,.$$

The left integrand contains the divergence of mean and eddy PV fluxes, and these could be integrated and written as a sum of fluxes across the lateral boundaries of the box. The net flux of PV out of the box by the mean flow and by the eddies must be balanced by generation of PV inside the box by heating/cooling at the surface and by frictional stresses acting tangentially along C. We will assume that the meridional flux of PV is primarily due to the mean flow and therefore that the second integrand on the left-hand side is neglected. We will further assume that the main contribution to the frictional term comes from the solid boundary. Also, if the boundary current is narrow and the surface buoyancy loss is spread evenly across the width of the basin, then the thermal forcing term is likely negligible compared to offshore eddy flux since the latter must supply the buoyancy that is lost in the interior. With these assumptions, the PV budget is

$$\int_0^L \int_{y_1}^{y_2} \int_{-H}^{0} \left(\frac{\partial \overline{v}\,\overline{q}}{\partial y} + \frac{\partial \overline{u'q'}}{\partial x} \right) dy\, dz\, dx = \oint_C \int_{-H}^{0} \mathbf{F}_r \cdot dz\, dl\,. \tag{2}$$

Although we have not specified the form of the frictional vector $\mathbf{F}_r$, we will assume that it opposes the flow

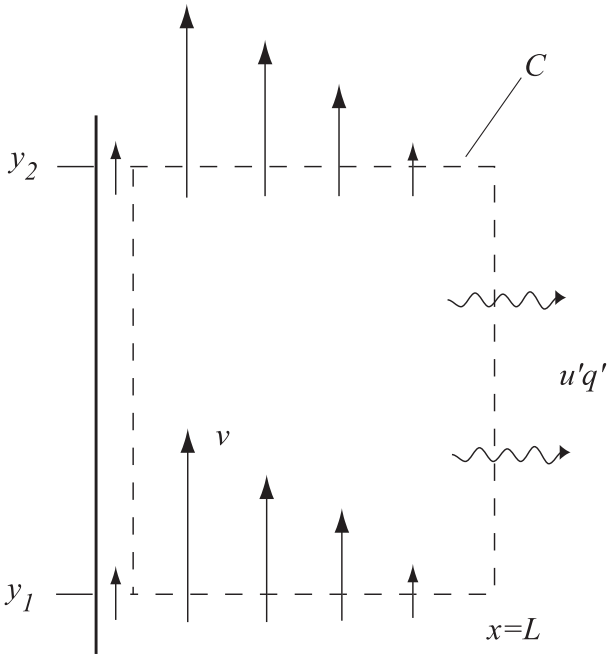

FIG. 9. A schematic diagram showing the structure of the boundary current.

along the wall. For a western boundary current as shown in Fig. 9, we anticipate the main frictional contribution will come from the segment of C corresponding to the wall so that $\oint_C \int_{-H}^{0} \mathbf{F}_r \cdot dz\, dl = -\int_{y_1}^{y_2} \int_{-H}^{0} F_r^{(y)}|_{x=L}\, dz\, dy$. A northward boundary current will be associated with a negative $F_r^{(y)}$, and (2) then indicates that the divergence of the potential vorticity flux (integrand on the left) must be positive. This is the situation that would exist for the northward flow of a linear, barotropic western boundary layer on a beta plane ($q = \beta y$) and with no eddies. If the same situation were postulated on the eastern boundary, the sign of the friction term would reverse but the divergence of the eddy flux would remain the same, so (2) would no longer hold. This reasoning would then constitute an argument for western intensification.

If q is dominated by the stretching term, with stratification weakening toward the north, so that $\partial/\partial z[f_0\rho_a/(\partial\rho_b/\partial z)]$ decreases in the northward direction, then the signs in the eddy-free version of (2) are self-consistent only if the friction comes from the eastern segment of the integration contour C. The geographic eastern boundary becomes the "dynamical" western boundary. In the Red Sea, where thermal convection in the north is expected to weaken stratification, it is possible that q will be dominated by βy in the south, and by the stretching term in the north, with dq/dy vanishing at some intermediate latitude. In an eddy-free environment, this would be the crossover

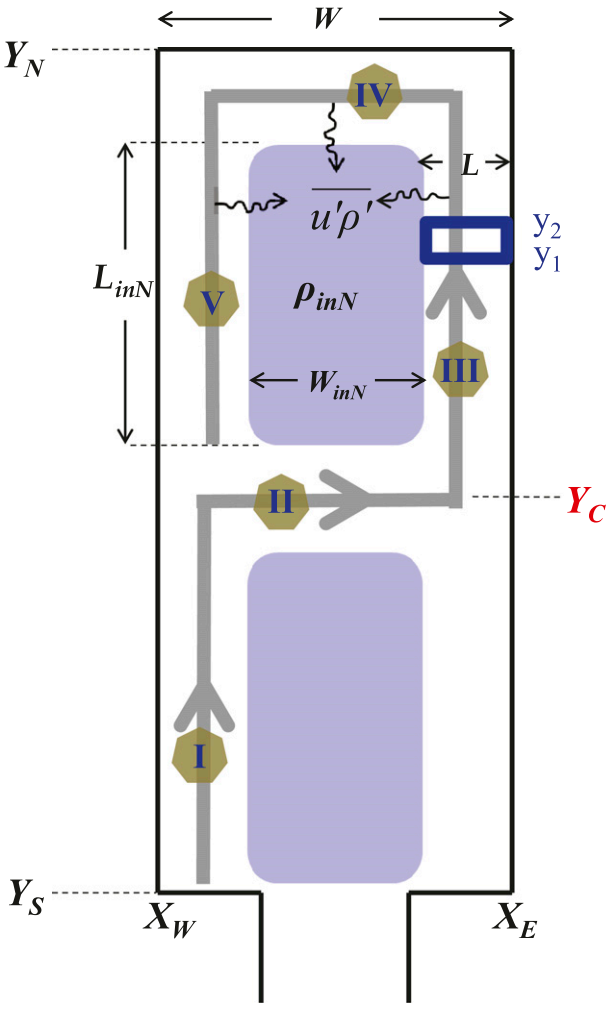

FIG. 10. A schematic diagram illustrating the boundary currents in the ad hoc analytical model.

latitude. However, the real situation is complicated by the presence of the eddy term in (2), and the general condition that must be satisfied at the crossover latitude is that the total advection (mean plus eddy) of PV is zero. This is the physical basis for the estimation of the crossover latitude, though further analysis and assumptions are required to write the fluxes in terms of the governing parameters of the model.

b. Assumptions

Figure 10 shows the assumed flow configuration and geometrical parameters used to produce the estimate of the crossover latitude Y_C. This picture is based on a number of assumptions:

1) The surface water that enters the Red Sea through the BAM moves northward along the western Red Sea boundary (current I) and crosses over to the

eastern boundary at latitude Y_C. (That the current should begin on the west coast is in agreement with the numerical model runs for nonzero β. In the actual Red Sea, the value of β is largest in the south, and the surface buoyancy forcing is weakest there. It stands to reason that the northward potential vorticity gradient will be dominated by β in the south, leading to westward intensification there.) To the north, the circulation is dominated by a set of cyclonic boundary currents (III, IV, and V).

2) The horizontal velocity components vary weakly with z over $0 \geq z \geq -H$ but rapidly go to zero below the base of this layer ($z = -H$).
3) The boundary layer dynamics are linear, meaning that contribution to q from relative vorticity ζ is weaker than the planetary contribution βy or that from the stretching term. This assumption is not always met in the numerical simulations, but it is invoked here to enable closure.
4) The surface buoyancy loss to the atmosphere in the interiors of the gyres is balanced by eddy buoyancy fluxes from boundary currents III, IV, and V into the interior. The importance of such eddy fluxes has been emphasized in a number of observations and model results from other marginal seas (e.g., Visbeck et al. 1996; Marshall and Schott 1999; Spall 2004, 2011, 2013; Pratt and Spall 2008; Isachsen and Nost 2012). We further assume that the eddy buoyancy flux is proportional to the mean boundary current velocity V_{bN} of boundary currents III, IV, and V (Stone 1972; Visbeck et al. 1996; Spall and Chapman 1998; Spall 2004) and to the density difference between the boundary current and the interior. For the eddy fluxes from boundary currents III, IV, and V into the interior of the northern gyres, this parameterization takes the form

$$\overline{u'\rho'} = cV_{bN}(\rho_{\text{in}N} - \rho_{bN}), \tag{3}$$

where c is a nondimensional coefficient representing the efficiency of buoyancy transport by the baroclinic eddy (c is related to the ratio of bottom slope to isopycnal slope; Spall 2004); ρ_{bN} is mean density of boundary currents III, IV, and V, averaged over its length, width, and depth; and $\rho_{\text{in}N}$ is the density of the interior region in the northern gyre, assumed to be constant. With this formulation the eddy buoyancy flux is constant along the length of the boundary layer.
5) V_{bN} is in thermal wind balance:

$$V_{bN} = \frac{Hg}{2\rho_0 f_C}\frac{\rho_{\text{in}N} - \rho_{bN}}{L}, \tag{4}$$

where L is the width of boundary current and is approximated using the width of bottom slope (80 km). The equation $f_C = f_0 + \beta Y_C$ defines the Coriolis parameter at the southern boundary of the northern gyre. Since the analytical model is applied in the northern gyre, f_C is used as a reference Coriolis parameter in (4) and the following calculations.
6) The wind stress is ignored, though we will later speculate on its effect.
7) The density varies linearly with depth over the surface layer of thickness H and has constant value ρ_0 below. Specifically,

$$\overline{\rho}(x,y,z) = \begin{cases} [1 - N^2(z+H)/g]\rho_0 + 2\langle\overline{\rho_a}\rangle(z+H)/H, & z \geq -H \\ \rho_0, & z < -H \end{cases}.$$

Thus, the background stratification $\rho_b(z) = [1 - N^2(z+H)/g]\rho_0$ (also the stratification of the resting state) has constant value N in the surface layer. The perturbation density $\overline{\rho_a} = 2\langle\overline{\rho_a}\rangle(z+H)/H$ also varies linearly with z, and its vertical average $\langle\overline{\rho_a}\rangle$ over the surface layer is a function of x and y. (The assumption of linearly varying density in the surface layer is in rough agreement with the numerical simulations, as suggested in Fig. 11.)

This concludes the list of assumptions. The goal now is to evaluate the terms in the left-hand side of (2), with the integration box located at the eastern boundary (as depicted by the blue rectangle in Fig. 10). We begin calculating the mean advection of PV. Its vertical average $\langle\overline{v}\,\overline{q}\rangle$ over the surface layer is

$$\langle\overline{v}\,\overline{q}\rangle = \frac{\overline{v}}{H}\int_{-H}^{0}\left(\beta y - \frac{f_C g}{\rho_0}\frac{\partial}{\partial z}\frac{\overline{\rho_a}}{N^2}\right)dz$$
$$= \overline{v}\left(\beta y - \frac{f_C g}{\rho_0 H}\frac{\overline{\rho_a}|_{z=0} - \overline{\rho_a}|_{z=-H}}{N^2}\right).$$

The density perturbation in the deep region is zero ($\overline{\rho_a}|_{z=-H} = 0$), and thus $\overline{\rho_a}|_{z=0} = 2\langle\rho_a\rangle$, so that

$$\langle\overline{v}\,\overline{q}\rangle = \overline{v}\beta y - \frac{2f_C g}{\rho_0}\frac{\langle\overline{\rho_a}\rangle}{HN^2}\overline{v}. \tag{5}$$

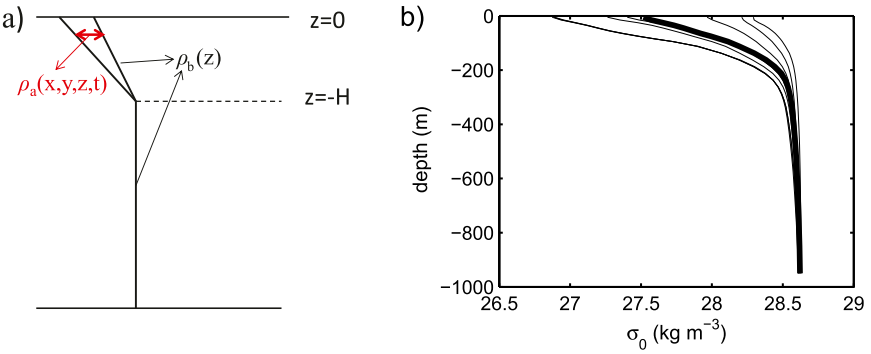

FIG. 11. (a) A schematic diagram of density profile in the analytical model. (b) Density profiles in EXPT0. The thick black line represents mean density profile, and thin black lines represent density profiles at different locations.

Similarly, the eddy flux of potential vorticity is

$$\langle \overline{u'q'} \rangle = -\frac{2f_C g}{\rho_0 H N^2} \overline{u' \langle \rho_a' \rangle}. \tag{6}$$

Angle brackets are dropped in the following calculation for convenience.

The divergence of the northward advection of density within an eastern boundary current is balanced by surface buoyancy loss to the atmosphere over the boundary current and zonal eddy fluxes of buoyancy from the boundary current into the interior, thus the buoyancy budget for boundary current III can be written as

$$\frac{\partial}{\partial y} \int_{X_E - L}^{X_E} \overline{v}\,\overline{\rho_a}\, dx - \overline{u'\rho_a'}\big|_{x = X_E - L} = \frac{LB_0(y)}{H}. \tag{7}$$

Here, $\overline{u'\rho_a'}$ is the zonal eddy buoyancy flux. A more detailed derivation of (7) appears in appendix A.

With the help of (5) and (6), the left-hand side of (2) can now be written as

$$\int_{X_E - L}^{X_E} \int_{y_1}^{y_2} \left(\frac{\partial \overline{v}\,\overline{q}}{\partial y} + \frac{\partial \overline{u'q'}}{\partial x} \right) dy\, dx = \int_{X_E - L}^{X_E} \int_{y_1}^{y_2} \left[\frac{\partial \overline{v}\beta y}{\partial y} - \frac{2f_C g}{\rho_0 H N^2} \left(\frac{\partial \overline{v}\,\overline{\rho_a}}{\partial y} + \frac{\partial \overline{u'\rho_a'}}{\partial x} \right) \right] dy\, dx$$

$$= \int_{y_1}^{y_2} \left[\frac{\partial}{\partial y} \int_{X_E - L}^{X_E} \overline{v}\beta y\, dx - \frac{2f_C g}{\rho_0 H N^2} \left(\frac{\partial}{\partial y} \int_{X_E - L}^{X_E} \overline{v}\,\overline{\rho_a}\, dx - \overline{u'\rho_a'}|x = {}_{X_E - L} \right) \right] dy. \tag{8}$$

If (7) is used to simplify the final expression in parentheses, and the result is substituted into (2), it follows that

$$L \int_{y_1}^{y_2} \left(\frac{\partial \overline{v}\beta y}{\partial y} - \frac{2f_C g B_0}{\rho_0 H^2 N^2} \right) dy = \iint_A \mathrm{curl}\mathbf{F}_r\, dx\, dy.$$

The integrand on the left-hand side represents the divergence of the advection of PV within the box. It includes contributions from mean and eddy fluxes. The predicted Y_C lies where the integrand vanishes, that is,

$$\frac{\partial \overline{v}\beta y}{\partial y} - \frac{2f_C g B_0(y)}{\rho_0 H^2 N^2} = 0 \quad (\text{at } y = Y_C), \tag{9}$$

where $B_0 = ay + b$.

To compute Y_C from (9), one needs to estimate the velocity $\overline{v}$ in terms of known parameters. This involves a series of algebraic steps that use the parameterization of baroclinic instability [(3)], the thermal wind condition [(4)], and the buoyancy budget for the northern gyre as a whole. The resulting septic equation for Y_C along with a prediction of the density difference between the boundary current and the interior are developed in appendix B [see (B3) and (B4)].

c. *PV constraints on the boundary currents and crossover latitude*

The predicted value of the crossover latitude Y_C is shown in Fig. 12 as a function of f_0, β, and the meridional

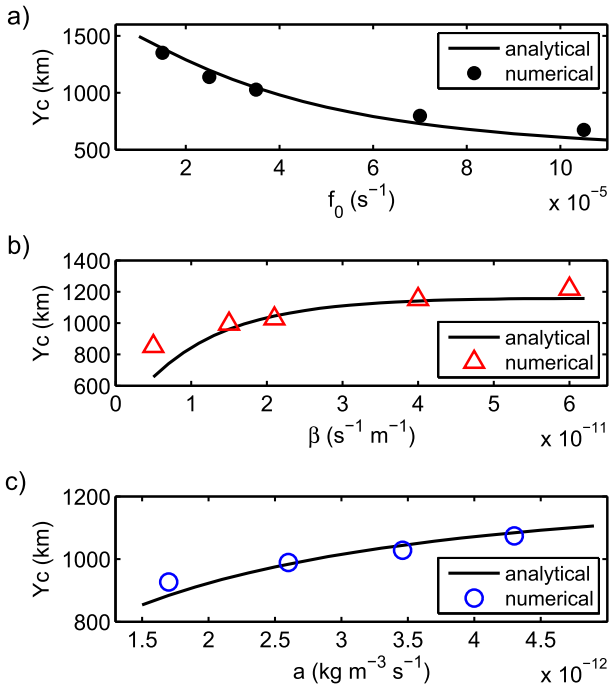

FIG. 12. Variations of crossover latitude due to variations in (a) f_0, (b) β, and (c) the meridional gradient of surface buoyancy loss a. The parameters for each experiment are given in Table 1.

gradient a of the surface buoyancy flux. In computing Y_C in the analytical model we have chosen N^2 as $2.2 \times 10^{-5}\,s^{-2}$, which is an average value in the model domain in EXPT0. The empirical constant c ranges from 0.008 to 0.03 through estimations in numerical experiments by using (3), and $c = 0.015$ is used in the analytical estimate. Sensitivity of the predicted Y_C to N^2 and c will be discussed below.

According to (9), the planetary PV advection is proportional to β, while the magnitude of the buoyancy loss term increases with f_0 and surface buoyancy loss. As a result, the crossover latitude is anticipated to increase with β and decrease with f_0, which is supported by Fig. 12. Equation (9) also suggests that the buoyancy loss term increases with the meridional gradient a of the surface buoyancy flux (as contained in the parameter $B_0 = ay + b$), and Fig. 12 confirms that when a decreases, the predicted and actual crossover latitude moves farther south. Essentially, a decrease in a causes the surface buoyancy losses to become stronger in the southern Red Sea and the contribution of stretching PV increases. Comparisons between the analytical prediction and numerical model for all model runs are shown in Fig. 13. The prediction tends to overestimate Y_C when Y_C is large and underestimate Y_C when Y_C is small. There is also a strong linear relationship between the predicted and numerical model values. The two agree with a least squares fit slope of 0.78 and a correlation coefficient of 0.97.

The comparisons of $\rho_{inN} - \rho_{bN}$ and V_{bN} are shown in Fig. 13. They also reveal good agreement between the numerical model and the ad hoc analytical model. The predicted and numerical model results of $\rho_{inN} - \rho_{bN}$ are linearly related with a correlation of 0.91 and a least squares fit slope of 1.06. According to (B3), $\rho_{inN} - \rho_{bN}$ increases with f_0 and β. The value $\rho_{inN} - \rho_{bN}$ also increases with the meridional gradient a of the surface buoyancy flux. This is because when a increases, the surface buoyancy losses become stronger in the northern Red Sea. Thus, a larger $\rho_{inN} - \rho_{bN}$ is required to generate larger eddy buoyancy fluxes to balance surface buoyancy losses in the interior region. The predicted and numerical model results of V_{bN} are linearly related

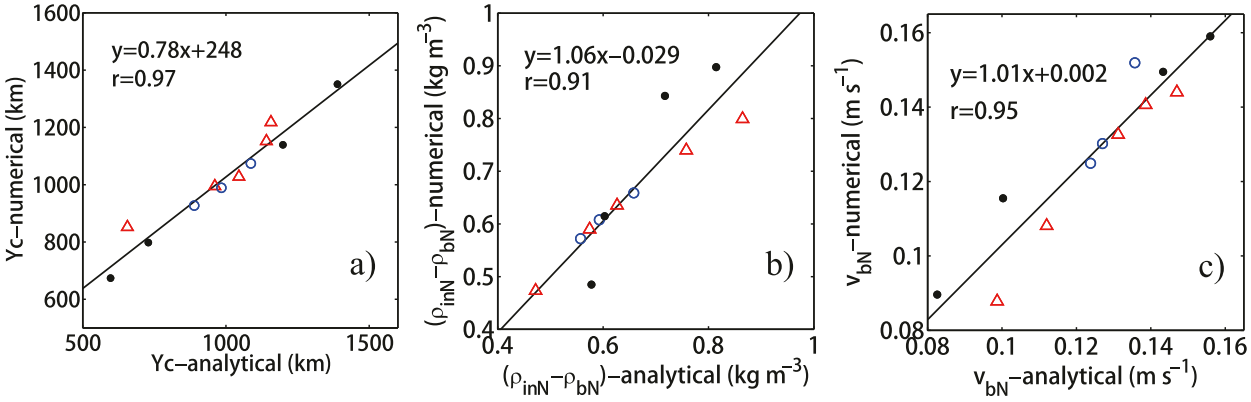

FIG. 13. Comparison of (a) crossover latitude, (b) density difference, and (c) boundary velocity between the analytical prediction and a series of numerical model results. The meaning of different types of symbols is described in Table 1. Black dots correspond to changing f_0, red triangles correspond to variable β, and blue circles correspond to the variable meridional gradient (a) of surface buoyancy flux. The black line is the least squares fit line to the points plotted in this figure.

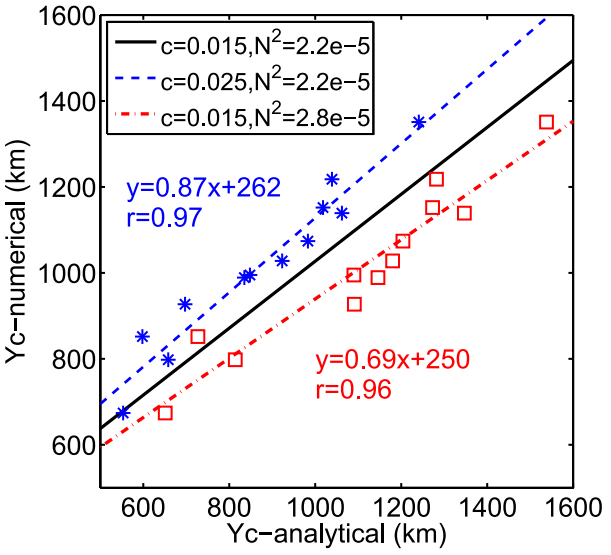

FIG. 14. Test of sensitivity of crossover latitude to c and N^2. The black line is the same as that in Fig. 13, which represents the ad hoc analytical model with $c = 0.015$ and $N^2 = 2.2 \times 10^{-5}\,s^{-2}$. The red dashed–dotted line and squares represent the ad hoc analytical model results with $c = 0.015$ and $N^2 = 2.8 \times 10^{-5}\,s^{-2}$. The blue dashed line and stars represent ad hoc analytical model results with $c = 0.025$ and $N^2 = 2.2 \times 10^{-5}\,s^{-2}$.

with a correlation of 0.95 and a least squares fit slope of 1.01. The term V_{bN} also increases with a, which can be explained by thermal wind relation [(4)]. Equation (4) also indicates that V_{bN} decreases with f_0 and β.

The predicted crossover latitude is somewhat sensitive to N^2. For example, when N^2 is chosen to be $2.8 \times 10^{-5}\,s^{-2}$ instead of $2.2 \times 10^{-5}\,s^{-2}$, the linear relation between the predicted and actual crossover latitude becomes $y = 0.69x + 250$, with a correlation coefficient of 0.96 (Fig. 14). The predicted crossover latitude is also somewhat sensitive to the efficiency coefficient c that arises in the parameterization of baroclinic instability. When c is changed from 0.015 to 0.025, the linear relation between the predicted and actual crossover latitude changes to $y = 0.87x + 262$, with a correlation coefficient of 0.97 (Fig. 14). We have kept N^2 and c fixed in the ad hoc analytical model. Although different choices of c and N^2 in the analytical model lead to different estimates of crossover latitude, the linear correlation coefficients remain as high as 0.96, as shown in Fig. 14.

4. Summary and conclusions

The buoyancy-driven circulation in an idealized Red Sea has been studied using a numerical and ad hoc analytical model on a β plane. A specific configuration of the numerical model is that the surface buoyancy fluxes have a constant meridional gradient such that freshwater and heat losses are stronger in the northern Red Sea than those in the southern Red Sea. The buoyancy loss in the idealized Red Sea is balanced by transports of freshwater and heat through the strait of Bab el Mandeb. In the time-mean circulation, the surface inflow enters the Red Sea, turns left, and moves northward on the western boundary until it reaches a certain latitude. The western boundary current then crosses the basin to the eastern boundary and continues its northward journey. The basic circulation consists of an anticyclonic gyre in the southern Red Sea and a cyclonic gyre in the northern Red Sea. This feature is different from the buoyancy-driven boundary circulation that arises in f-plane, semienclosed basins where the surface inflow from the open ocean tends to flow cyclonically around the boundaries (e.g., Spall 2004).

To understand what controls the crossover latitude of the western boundary current in the idealized Red Sea, a series of numerical experiments were carried out with the variables f_0, β, and meridional surface buoyancy flux gradient. The results of these experiments indicate that the crossover latitude of the western boundary current moves farther north with smaller f_0, larger β, or a larger meridional gradient of surface buoyancy fluxes. An ad hoc analytical prediction based on thermal wind relation, the density equation, and PV dynamics exhibits the correct parameter tendencies and agrees reasonably well with the numerical values of Y_C. Although the theory overestimates (underestimates) Y_C for large (small) Y_C, it exhibits a very strong linear relationship with the actual values. The central thesis of the model is that crossover will occur where the total advection of PV, including offshore eddy fluxes, in the boundary current vanishes. This constraint is most easily cast as a circulation integral about a small element of the boundary current, which equates the divergence of the potential vorticity flux to the friction along the boundary wall. Agreement between the signs of each contribution determines whether the dynamical western boundary is the geographical eastern or western boundary. The advection of planetary PV tends to encourage geographic western boundary currents, while the advection of the stretching PV (which is related to buoyancy loss terms) tends to encourage geographic eastern boundary currents. Our theory also produces an estimate for the density difference between the boundary currents and the interior in the northern gyre, and this is in reasonably good agreement with the model results.

Our model shares some elements with at least two other studies of eastern boundary currents in midlatitude oceans. The aforementioned work by MSK86

centers on a semi-infinite ocean with an eastern boundary and with buoyancy and wind forcing. The buoyancy forcing increases to the north, producing a sea surface that slopes down toward the north and a geostrophically balanced flow toward the east. This flow is brought to zero at the eastern boundary by a boundary layer that relies on thermal diffusion to achieve a vorticity balance. The boundary current has poleward surface flow, with surface sinking, and there is weaker, equatorward undercurrent. The model results include cases of steady forcing along with cases of seasonal forcing, but the domain of interest lies to the south of the critical latitudes for the first two baroclinic, Rossby wave modes in all cases. Although there is no western boundary and nothing like a crossover jet, the structure of the eastern boundary current may share some elements with that in our model, which also has poleward surface flow with an opposing undercurrent. (This aspect is lost in the averaging that we do over the upper 200 m of our model but is worthy of further investigation.)

Pedlosky and Spall (2005, hereinafter PS05) analyze a buoyancy-forced, two-layer circulation in a rectangular domain. The PS05 model involves steady, β-plane flow, so the whole domain essentially lies to the south of the relevant Rossby wave critical latitude. The buoyancy forcing, which is introduced as a cross-interface velocity, increases linearly to the north and produces the same eastward geostrophic flow as in MSK86. The model also admits an eastern thermal ''boundary layer,'' in which sinking takes place, but in the asymptotic setting explored by PS05, this layer covers the interior. The linear, quasigeostrophic analytical model has a southward western boundary current at all latitudes within the domain, with smooth, eastward flow in the interior not crossover jet. Primitive equation numerical simulations are also presented, and one of these produces a closed, cyclonic gyre in the north, similar to that seen in our simulations (e.g., Fig. 4). But again, there is no distinct crossover jet. The discrepancy between PS05 and this study might be because of the model configuration. The inflow transport in their analytical model is weak by assumption and is specified, while the inflow transport in our study is part of the solution. The buoyancy forcing in our model is imposed as a surface buoyancy flux, whereas their forcing is imposed by restoring an interface to some predetermined shape. Thus, the resulting spatial pattern of forcing is different. In addition, the sloping boundary in our model may have a substantial influence on the physics of the boundary layers.

Buoyancy-driven circulation in the idealized Red Sea consists of an anticyclonic boundary circulation in the southern Red Sea and a cyclonic boundary circulation in the northern Red Sea. This circulation pattern is similar in some respects to that of the subtropical and subpolar gyres of the North Atlantic and North Pacific. However, it is generally agreed that these gyres are driven by wind, whereas the Red Sea circulation is primarily determined by buoyancy forcing (Sofianos and Johns 2003).

The crossover latitude moves southward in the numerical experiment with surface wind stress in Sofianos and Johns (2003). Further to the issue of wind forcing, it is natural to ask how wind might influence the crossover latitude. The simplest way of introducing a wind stress would be to incorporate it as a body force $\tau/\rho H$, evenly distributed over the depth of the upper 200 m. The function (2) then becomes

$$\int_0^L \int_{y_1}^{y_2} \int_{-H}^0 \left[\frac{\partial \overline{v}\,\overline{q}}{\partial y} + \frac{\partial \overline{u'q'}}{\partial x} - \mathrm{curl}\left(\frac{\tau}{\rho H}\right) \right] dy\, dz\, dx = \oint_C \int_{-H}^0 \mathbf{F}_r \cdot dz\, dl .$$

The crossover occurs where the friction term on the right vanishes, as before. If the wind stress curl is negative, the corresponding term agrees in sign with the term involving β (hidden in $\overline{v}\,\overline{q}$), and this would tend to move the crossover latitude northward, provided that the eddy flux term remains the same. The wind stress curl in winter in the southern Red Sea in Sofianos and Johns (2003) is positive. Thus, the crossover latitude moves southward in their study.

Although our formal prediction of the crossover latitude differs from what Sofianos and Johns (2003) suggest, with ours based on a steady state and theirs based on seasonal time dependence, the underlying mechanisms share some common elements. Both involve potential vorticity dynamics, and both contemplate a basin in which the beta effect, westward propagation of Rossby waves, and westward intensification dominate in the southern portion. In Sofianos and Johns (2003), β decreases in the northward direction, and there exists a latitude beyond which propagation of long Rossby waves at the annual frequency is not supported. In our scenario, the beta effect is reversed at higher latitude by vortex stretching due to diverging isopycnals and possibly by offshore eddy fluxes of potential vorticity. In our study, both the ad hoc analytical model and numerical model suggest that it is the

competition between the advection of planetary vorticity and the buoyancy loss term in the PV budget that determines the crossover latitude.

Acknowledgments. We have benefited from talking with Tom Farrar, Jiayan Yang, Paola Rizzoli, and Mike Spall. This work is supported by Award USA 00002, KSA 00011, and KSA 00011/02 made by King Abdullah University of Science and Technology (KAUST), by National Science Foundation Grants OCE0927017, OCE1154641, and OCE85464100, and by the Woods Hole Oceanographic Institution Academic Program Office.

APPENDIX A

Simplification of the Density Equation

The density equation can be written as

$$\frac{\partial \overline{u}\,\overline{\rho_a}}{\partial x}+\frac{\partial \overline{v}\,\overline{\rho_a}}{\partial y}+\frac{\partial \overline{w}\,\overline{\rho_a}}{\partial z}+\frac{\partial \overline{u'\rho_a'}}{\partial x}+\frac{\partial \overline{v'\rho_a'}}{\partial y}+\frac{\partial \overline{w'\rho_a'}}{\partial z}=\frac{B_0}{H}.$$

We now integrate this equation vertically over the thickness H of the upper layer and also from the outer edge $x = X_E - L$ of the eastern boundary current to the position $x = X_E$ of the eastern wall. We will assume that the vertical velocity vanishes or is negligibly small at $z = 0$ and also at $z = -H$ (consistent with the assumption that H is constant). We also set $u = u' = 0$ at the wall, and we further assume that the northward advection of density by the time-averaged flow is much larger than the northward eddy flux of density $\overline{v}\,\overline{\rho_a} \gg \overline{v'\rho_a'}$. This all leads to (7).

APPENDIX B

Development of the Relationship for the Critical Latitude Y_C

To derive the prediction for Y_C, we begin by approximating the velocity in (9) with the average velocity V_{bN} in boundary currents III, IV, and V. Use of the thermal wind relation [(4)] for V_{bN} then leads to

$$\frac{\beta N^2 H^2}{4f_C^2}(\rho_{\mathrm{in}N}-\rho_{bN})=\frac{LB_0(Y_C)}{H}, \tag{B1}$$

where $B_0(Y_C) = aY_C + b$. To get an expression for $(\rho_{\mathrm{in}N} - \rho_{bN})$, we consider the buoyancy budget for the northern gyre as a whole. As suggested in Fig. 10, the sea surface buoyancy loss in the interior region (shaded in blue in Fig. 10) in the northern gyre is assumed to be balanced by lateral eddy fluxes originating from boundary currents III, IV, and V. Thus, the buoyancy budget can be written as

$$[2L_{\mathrm{in}N}(Y_C)+W_{\mathrm{in}N}]H\overline{u'\rho'}=\int_{A_N}B_0\,dA=W_{\mathrm{in}N}B_{TN}(Y_C), \tag{B2}$$

where $L_{\mathrm{in}N}(Y_C) = Y_N - (3L/2) - Y_C$ and $W_{\mathrm{in}N}$ are the length and width of the interior region in the northern gyre; $A_N = L_{\mathrm{in}N}W_{\mathrm{in}N}$ is the area of interior region; H is the vertical scale of the boundary current; and

$$B_{TN}(Y_C)=\int_{Y_C+L/2}^{Y_N-L}B_0\,dy.$$

If (B2) is combined with the thermal wind relation [(4)] for V_{bN} and with the parameterization of baroclinic instability [(3)], one obtains an expression for the density difference between the boundary current and the interior:

$$\rho_{\mathrm{in}N}-\rho_{bN}=\sqrt{\frac{2\rho_0 f_C L W_{\mathrm{in}N}B_{TN}}{cH^2 g(2L_{\mathrm{in}N}+W_{\mathrm{in}N})}}. \tag{B3}$$

Substitution for the density difference in (B1) leads to

$$\frac{\beta N^2H^2}{4f_C(Y_C)^2}\sqrt{\frac{2\rho_0 f_C(Y_C)LW_{\mathrm{in}N}B_{TN}(Y_C)}{cg[2L_{\mathrm{in}N}(Y_C)+W_{\mathrm{in}N}]}}=LB_0(Y_C). \tag{B4}$$

Given that B_0 and $L_{\mathrm{in}N}$ are linear in Y_C, and that B_{TN} is quadratic in Y_C, it follows that (B4) is essentially a septic equation for Y_C, though in practice it is solved in the above form.

REFERENCES

Biton, E., H. Gildor, and W. R. Peltier, 2008: Red Sea during the Last Glacial Maximum: Implications for sea level reconstruction. *Paleoceanography,* **23,** PA1214, doi:10.1029/2007PA001431.

——, ——, G. Trommer, M. Siccha, M. Kucera, M. T. J. van der Meer, and S. Schouten, 2010: Sensitivity of Red Sea circulation to monsoonal variability during the Holocene: An integrated data and modeling study. *Paleoceanography,* **25,** PA4209, doi:10.1029/2009PA001876.

Bower, A., 2010: Cruise report—R/V Aegaeo KAUST leg1 northeastern Red Sea, 16-29 March 2010. WHOI Tech. Rep. WHOI-KAUST-CTR-2010-01, 28 pp.

——, and Y. Abualnaja, 2011: Cruise report—R/V Aegaeo KAUST leg1 eastern Red Sea, 15 September-10 October 2011. WHOI Tech. Rep. WHOI-KAUST-CTR-2011-01, 25 pp.

——, and J. Farrar, 2015: Air-sea interaction and horizontal circulation in the Red Sea. *The Red Sea: The Formation,*

Morphology, and Environment of a Young Ocean Basin, N. Rasul and I. Stuart, Eds., Springer, 329–342.

Chen, C., and Coauthors, 2014: Process modeling studies of physical mechanisms of the formation of an anticyclonic eddy in the central Red Sea. *J. Geophys. Res. Oceans,* **119,** 1445–1464, doi:10.1002/2013JC009351.

Clifford, M., C. Horton, J. Schmitz, and L. H. Kantha, 1997: An oceanographic nowcast/forecast system for the Red Sea. *J. Geophys. Res.,* **102,** 25 101–25 122, doi:10.1029/97JC01919.

Eshel, G., and N. H. Naik, 1997: Climatological coastal jet collision, intermediate water formation, and the general circulation of the Red Sea. *J. Phys. Oceanogr.,* **27,** 1233–1257, doi:10.1175/1520-0485(1997)027<1233:CCJCIW>2.0.CO;2.

Griffies, S. M., and R. W. Hallberg, 2000: Biharmonic friction with a Smagorinsky-like viscosity for use in large-scale eddy-permitting ocean models. *Mon. Wea. Rev.,* **128,** 2935–2946, doi:10.1175/1520-0493(2000)128<2935:BFWASL>2.0.CO;2.

Isachsen, P. E., and O. A. Nost, 2012: The air sea transformation and residual overturning circulation within the Nordic Seas. *J. Mar. Res.,* **70,** 31–68, doi:10.1357/002224012800502372.

Maillard, C., 1974: Eaux intermediaires et formation d'eau profonde en Mer Rouge. *L'Oceanographie Physique de la Mer Rouge,* CNEXO, 105–133.

Marshall, J., and F. Schott, 1999: Open-ocean convection: Observations, theory, and models. *Rev. Geophys.,* **37,** 1–64, doi:10.1029/98RG02739.

——, C. Hill, L. Perelman, and A. Adcroft, 1997: Hydrostatic, quasi-hydrostatic, and nonhydrostatic ocean modeling. *J. Geophys. Res.,* **102,** 5733–5752, doi:10.1029/96JC02776.

McCreary, J. P., S. R. Shetye, and P. K. Kundu, 1986: Thermohaline forcing of eastern boundary currents: With application to the circulation off the west coast of Australia. *J. Mar. Res.,* **44,** 71–92, doi:10.1357/002224086788460184.

Morcos, S., 1970: Physical and chemical oceanography of the Red Sea. *Oceanogr. Mar. Biol.,* **8,** 73–202.

——, and G. F. Soliman, 1974: Circulation and deep water formation in the northern Red Sea in winter. *L'Oceanographic Physique de la Mer Rouge,* CNEXO, 91–103.

Murray, S. P., and W. Johns, 1997: Direct observations of seasonal exchange through the Bab el Mandeb strait. *Geophys. Res. Lett.,* **24,** 2557–2560, doi:10.1029/97GL02741.

Pedlosky, J., 1996: *Ocean Circulation Theory.* Springer-Verlag, 453 pp.

——, and M. A. Spall, 2005: Boundary intensification of vertical velocity in a β-plane basin. *J. Phys. Oceanogr.,* **35,** 2487–2500, doi:10.1175/JPO2832.1.

Phillips, O. M., 1966: On turbulent convection currents and the circulation of the Red Sea. *Deep-Sea Res. Oceanogr. Abstr.,* **13,** 1149–1160.

Pratt, L. J., and M. Spall, 2008: Circulation and exchange in choked marginal seas. *J. Phys. Oceanogr.,* **38,** 2639–2661, doi:10.1175/2008JPO3946.1.

Quadfasel, D., and H. Baudner, 1993: Gyre-scale circulation cells in the Red-Sea. *Oceanol. Acta,* **16** (3), 221–229.

Siddall, M., D. A. Smeed, S. Matthiesen, and E. J. Rohling, 2002: Modelling the seasonal cycle of the exchange flow in Bab El Mandab (Red Sea). *Deep-Sea Res. I,* **49,** 1551–1569, doi:10.1016/S0967-0637(02)00043-2.

Smeed, D. A., 1997: Seasonal variation of the flow in the strait of Bab al Mandab. *Oceanol. Acta,* **20** (6), 773–781.

——, 2000: Hydraulic control of three-layer exchange flows: Application to the Bab al Mandab. *J. Phys. Oceanogr.,* **30,** 2574–2588, doi:10.1175/1520-0485(2000)030<2574:HCOTLE>2.0.CO;2.

——, 2004: Exchange through the Bab al Mandab. *Deep-Sea Res. II,* **51,** 455–474, doi:10.1016/j.dsr2.2003.11.002.

Sofianos, S. S., and W. E. Johns, 2003: An Oceanic General Circulation Model (OGCM) investigation of the Red Sea circulation: 2. Three-dimensional circulation in the Red Sea. *J. Geophys. Res.,* **108,** 3066, doi:10.1029/2001JC001185.

——, ——, and S. P. Murray, 2002: Heat and freshwater budgets in the Red Sea from direct observations at Bab el Mandeb. *Deep-Sea Res.,* **49,** 1323–1340.

Spall, M. A., 2004: Boundary currents and water mass transformation in marginal seas. *J. Phys. Oceanogr.,* **34,** 1197–1213, doi:10.1175/1520-0485(2004)034<1197:BCAWTI>2.0.CO;2.

——, 2011: On the role of eddies and surface forcing in the heat transport and overturning circulation in marginal sea. *J. Climate,* **24,** 4844–4858, doi:10.1175/2011JCLI4130.1.

——, 2013: On the circulation of Atlantic Water in the Arctic Ocean. *J. Phys. Oceanogr.,* **43,** 2352–2371, doi:10.1175/JPO-D-13-079.1.

——, and D. C. Chapman, 1998: On the efficiency of baroclinic eddy heat transport across narrow fronts. *J. Phys. Oceanogr.,* **28,** 2275–2287, doi:10.1175/1520-0485(1998)028<2275:OTEOBE>2.0.CO;2.

Stone, P., 1972: A simplified radiative–dynamical model for the static stability of rotating atmospheres. *J. Atmos. Sci.,* **29,** 405–418, doi:10.1175/1520-0469(1972)029<0405:ASRDMF>2.0.CO;2.

Vercelli, E., 1927: Richerche di oceanografia fisica eseguite della R. N. AMMIRAGLIO MAGNAGHI (1923– 24), 4, la temperatura e la salinita. *Ann. Idrogr.,* **11,** 1–66.

Visbeck, M., J. Marshall, and H. Jones, 1996: Dynamics of isolated convective regions in the ocean. *J. Phys. Oceanogr.,* **26,** 1721–1734, doi:10.1175/1520-0485(1996)026<1721:DOICRI>2.0.CO;2.

Yao, F., I. Hoteit, L. J. Pratt, A. S. Bower, P. Zhai, A. Köhl, and G. Gopalakrishnan, 2014a: Seasonal overturning circulation in the Red Sea: 1. Model validation and summer circulation. *J. Geophys. Res. Oceans,* **119,** 2238–2262, doi:10.1002/2013JC009004.

——, ——, ——, ——, A. Köhl, G. Gopalakrishnan, and D. Rivas, 2014b: Seasonal overturning circulation in the Red Sea: 2. Winter circulation. *J. Geophys. Res. Oceans,* **119,** 2263–2289, doi:10.1002/2013JC009331.

Zhai, P., and A. S. Bower, 2013: The response of the Red Sea to a strong wind jet near the Tokar Gap in summer. *J. Geophys. Res. Oceans,* **118,** 422–434, doi:10.1029/2012JC008444.